Potentiometric Parameterization of Dinaphtho[2,3-b:2′,3′-f]thieno[3,2-b]thiophene Field-Effect Transistors with a Varying Degree of Non-Idealities

Chang-Hyun Kim, Suzanne Thomas, Ji Hwan Kim, Martin Elliott, J. Emyr Macdonald, and Myung-Han Yoon*

Dr. C.-H. Kim, J. H. Kim, Prof. M.-H. Yoon
School of Materials Science and Engineering, Gwangju Institute of Science and Technology, Gwangju 61005, Republic of Korea
E-mail: mhyoon@gist.ac.kr
Dr. C.-H. Kim
Research Institute for Solar and Sustainable Energies, Gwangju Institute of Science and Technology, Gwangju 61005, Republic of Korea
S. Thomas, Prof. M. Elliot, Prof. J. E. Macdonald
School of Physics and Astronomy, Cardiff University, The Parade, Cardiff CF24 3AA, UK

Organic transistors with different structures are investigated to address the applicability and reliability of parameter extraction. A dinaphtho[2,3-b:2′,3′-f]thieno[3,2-b]thiophene channel is coupled with pristine or functionalized gold bottom and top contacts to reveal a geometrical impact on the device performance and non-idealities. Scanning Kelvin probe microscopy is employed as a key method to quantify the channel and contact potential *in-operando*. Taking full account of the contact effects and including an explicit threshold voltage in calculation are shown to be critical to access the intrinsic carrier mobility, while simple derivative-based extraction may over- or underestimate it. Further analytical developments correlate individual physical parameters, leading to the discovery that pentafluorobenzenethiol self-assembled on gold predominantly affects the carrier mobility rather than the injection barrier.

1. Introduction

New technologies need support from robust assessment principles for people to precisely diagnose performance bottlenecks and to establish rational strategies for improvements. As the field of organic electronics develops into maturity, there has been increasingly intensive discussion on how reliably device behaviors are measured, interpreted, reproduced, and advertised.[1-3] Since the parameters of interest for organic photovoltaics (i.e. open-circuit voltage, short-circuit current, and fill factor) are all *phenomenological* parameters (i.e. a given current-voltage curve is unambiguously reduced to a set of parameters), a focus is naturally placed on the importance of recording such a curve in a fully standardized manner with, for instance, no extra light, heat, or active areas involved.[4] In contrast, widely discussed parameters (i.e. charge-carrier mobility and threshold voltage, V_T) for organic field-effect transistors (OFETs) are *model* parameters, meaning that the numbers are inherently dependent on the model used as well as the procedure followed to implement this model.[5,6] Therefore, the lack of consensus may lead to discrepancies in parameters extracted even from the same current-voltage curve.

In 2004, Horowitz and co-workers summarized and extended a series of their earlier works to clarify non-idealities, or disagreement with metal-oxide-semiconductor field-effect transistors (MOSFETs) in OFET devices.[7] As illustrated here, gate-voltage (V_G) dependence of mobility and existence of the contact resistances (R_c) are two common and theoretically justifiable sources of deviations from ideal MOSFET characteristics. Until recently, many experimental studies employed techniques such as the transmission-line method (TLM) or gated four-point probe measurements (gFPP), which can in principle directly probe these phenomena by separating the channel and contact properties.[8-14] In our view, the reported data bring strong evidence for the pronounced variability in relative strengths, and voltage- or structure dependence of the contact and channel effects, which makes different theoretical frameworks often necessary to understand different devices. Nonetheless, the MOSFET

2

current-voltage model has been employed quite universally for simple parameter extraction. In 2016, Gundlach and co-workers used impedance spectroscopy to systematically address mobility overestimation in rubrene single-crystal transistors,[15] an issue that in fact originates from neglecting R_c and/or non-contextually adopting simplified equations. In this context, it is timely to critically re-assess basic assumptions of the device parameters, specific behavioral non-idealities, and associated calculation issues. Ideally, growing efforts into such a process will be transformed into carefully thought-out and broadly accepted practices for OFET research.

In this article, we report on the use of scanning Kelvin probe microscopy (SKPM) and correlated analysis aimed at generalizable parameterization. SKPM is a powerful, surface-sensitive technique that can directly probe critical resistive pathways in OFETs to quantify material- and interface-related parameters. Furthermore, SKPM holds some advantages over the TLM or gFPP in that neither averaging over multiple devices nor integration of metal probes into the channel is necessary. The semiconductor of choice is dinaphtho[2,3-b:2′,3′-f]thieno[3,2-b]thiophene (DNTT), whose deep-lying highest-occupied molecular orbital (HOMO) and outstanding hole mobility provide a particularly intriguing platform for tackling the interplay between charge injection and transport. Unlike previous reports of potential measurements on DNTT transistors,[16-18] our primary questions are how to understand attributes of different device structures and on how extractable parameters are physically correlated. More importantly, our systematic flow of analysis exemplifies a robust evaluation scheme that not only emphasizes the final values but also puts significant efforts in validation and cross-check of the model that produces these values.

2. Results and Discussion

2.1. Device Performance

DNTT OFETs with three technologically relevant geometries were constructed as depicted in **Figure 1**a. Here, the Au bottom-contact (BC) and top-contact (TC) devices represent the

coplanar and staggered configuration, respectively, in the presence of a bottom-gate that is usually employed for a vacuum-processed molecular semiconductor.[5] There is another group of BC devices with self-assembled monolayer (SAMs) of pentafluorobenzenethiol (PFBT) on Au (BC-SAMs), with which we intend to elucidate the effect of interface functionalization. For all OFETs, we incorporated a bilayer dielectric of poly(methylmethacrylate) (PMMA) and SiO_2, to benefit from the surface inertness of the former and the strong insulation of the latter. All layers other than Au were prepared with the same process parameters, and the DNTT films for all devices were evaporated in a single process run, to ensure that observed differences will find their root cause in the contact geometries and metal/organic interfaces alone. Figure 1b shows the chemical structure of DNTT, PMMA, and PFBT.

As an aggregated performance indicator, saturation-regime transfer characteristics of OFETs were recorded. The results in Figure 1c evidence the high-quality switching of our devices with small hysteresis, a current on-off ratio over 10^6, and turning-on at V_G close to 0 V. Indeed, deliberately introduced changes in geometry resulted in noticeable variations in performance, mainly seen at the on-state drain current (I_D). At this point, our focus goes to exploring intermediate manifestations between the variable (geometry) and outcome (performance), rather than simply pushing the performance of the most promising structure. In this context, output analysis in Figure 1d reveals an important aspect (the raw data for this figure are in Figure S1, Supporting Information); moving from TC to BC not only leads to inferior performance, but also introduces more pronounced non-idealities. While the TC device shows a nearly textbook-like linear-to-saturation transition, the BC and BC-SAMs devices show super-linearly increasing I_D at low drain voltage (V_D) and restricted saturation at high V_D. The output differential conductance more directly visualizes related issues;[19] Figure 1d (inset) indicates that it does not monotonically decrease in the case of BC-SAMs, and there is even a strong initial rise for the BC device. Such non-linearity is often considered as a manifestation of R_c, accounted for by a diode-like parasitic element that gradually facilitates

current injection upon increasing V_D.[20,21] However, field enhancement of carrier mobility may also generate similar shapes,[22] thus the presence of R_c in our OFETs still remains a question (to be answered in Section 2.3).

We briefly note that experiments with pentacene, a more classical semiconductor, showed less dramatic performance variation than that obtained with DNTT (Figure S2, Supporting Information). This verification strengthens our hypothesis that it is the remarkably high ionization potential (IP) of DNTT (ca. 5.4 eV) that maximizes injection-related problems, making contact assessment a particularly critical task for devices comprising this material.[23] Pentacene generally develops a polycrystalline state that is very similar to that of DNTT, but its lower IP (ca. 5.1 eV) makes the HOMO level much more approachable by the Fermi level of common high-work-function metals. Notwithstanding, it is important to point out that the high IP is a major contributor to the exceptional air stability of DNTT.[24]

2.2. Film Morphology

Recalling our previous simulation results, geometrical confinement of charge distribution can be a basic source of the observed variation; a narrow low-carrier-density zone at the electrode/channel edge was shown to degrade the performance of coplanar structures compared to staggered ones, even with the same semiconductor and interface parameters.[25,26]

Figure 2 provides clear evidence that morphology is another key contributor to the difference between the TC and BC geometries. The atomic-force microscopy (AFM) images here show that, despite the nominally identical DNTT deposition, there are striking differences in the final film microstructure. Figure 2 includes images taken separately on the electrode (DNTT on Au or PFBT-coated Au) and on the channel (DNTT on PMMA) for the BC and BC-SAMs samples, and a single channel image for the TC device where the entire film sits on PMMA. The BC electrode image (Figure 2a, right) features small, densely-packed grains that can be attributed to the strong substrate-molecule interaction;[27] a similar morphology has been reported in pentacene on Au.[28] Comparison of this image to the BC-

SAMs electrode image (Figure 2b, right) discloses one effect of the SAMs. PFBT molecules are known to make the Au surface more hydrophobic,[29] and this can explain the build-up of smaller grains on our SAM-modified metal electrode. Another interesting finding is that, despite the same underlying surface of PMMA, the channel morphologies somewhat reflect the existence and chemistry of the coplanar source/drain electrodes. Although visibly larger than those above the electrode, the DNTT grains on the BC device's channel (Figure 2a, left) are much smaller than those on the corresponding TC OFET channel (Figure 2c). We infer that this particular growth condition affords substantial diffusive motion of arriving molecules,[27] to the point that lateral interaction of crystallites on Au and PMMA culminates in the channel morphology intermediate between that on the electrode and that on the 'free' PMAA surface. Similarly, the channel morphology in the BC-SAMs device (Figure 2b, left) can be viewed as a slightly released and planarized state of the adjacent electrode morphology.

The film formation in the TC device seems to be apparently free from this mechanism, and Figure 2c exhibits substantially larger dendritic grains. Here, clear terrace-like structures are observed, as confirmed by simple histogram analysis of heights for the two rectangular zones marked as A and B (Figure 2d,e). The emergence and periodicity of multiple peaks manifests a high degree of ordering and layer-by-layer growth mode (five and four layers for the zone A and B, respectively). The peak-to-peak distances represent vertical interlayer distances, which in this case roughly approximate to the molecular length or c-axis dimension in the triclinic unit cell of the DNTT crystal (Figure 2d, inset).[30] Therefore, it can be inferred that the channel is mainly composed of molecules that are standing up on PMMA [or (001) plane parallel to the substrate], which is expected to favor in-plane charge transport.[31]

2.3. Parameter Extraction

SKPM is able to sequentially perform high-resolution recording of surface topography and potential, allowing for the systematic correlation between physical layers, their interfaces, and

electrostatics (Figure S3, Supporting Information).[32] This technique is used here to directly probe our OFETs' electrical conduction path under current-carrying conditions.

The result for the TC device, recorded at an intermediate V_D, shows saturation-to-linear regime transition upon increasing V_G (**Figure 3**a). More importantly, it is an additional confirmation that the TC behavior can be described as nearly ideal, because the applied V_D is solely maintained by the channel. In contrast, the linear-regime potential profiles from the BC and BC-SAMs transistors manifest the emergence of non-negligible potential drops at the electrode/channel interfaces (Figure 3b), in good agreement with computational prediction.[25] The profiles here at $V_G = 0$ V reflect the intrinsically dielectric-like character of the organic semiconductor in the absence of injected charges,[5] which makes the contact effect practically invisible (i.e. bulk resistivity becomes dominant). In all the other profiles in Figure 3b, the applied V_D is dropped partially at the channel and also at the contacts, with

$$V_D = V_{\text{ch}} + V_c, \tag{1}$$

where V_{ch} and V_c are the potential drops across the channel and the combined source and drain contacts, respectively.

To start parameterizing, we first extracted V_T. Some of the measured linear-regime transfer characteristics exhibited a curved shape, which makes the linear extrapolation method difficult to rely upon.[33] We therefore used the second-derivative method by which V_T appears as the position of a uniquely defined peak (Figure S4, Supporting Information).[34] Next, R_c and the 'intrinsic' channel resistance R_{ch} were calculated by the relationships

$$R_c = \frac{V_c}{I_D}, \tag{2}$$

and

$$R_{\text{ch}} = \frac{V_{\text{ch}}}{I_D}. \tag{3}$$

Now, the intrinsic mobility μ_{ch} is accessible by assuming a normal linear-regime channel conductance, and with the use of predetermined V_T, as

$$\mu_{ch} = \frac{1}{R_{ch}} \times \frac{L}{WC(V_G - V_T)}, \qquad (4)$$

where W is the channel width, L is the channel length, and C is the gate dielectric capacitance per unit area.

Figure 3c (main panel) shows the modulation of the width-normalized R_c by V_G. The horizontal axis is drawn here as the effective overdrive voltage V_G-V_T that is directly proportional to the accumulated charge density, thus enabling comparison between samples on a common physical basis. Also, although often overlooked, the values of R_c based on the linear-regime assumption should be strictly discussed in this regime of operation. For this reason, we systematically disregarded values at certain V_G, and included in Figure 3c only those that satisfy V_G-$V_T < V_D$. When comparing the BC and BC-SAMs samples, the addition of SAMs brought significant reduction in R_c. At first glance, this might be attributed to the substantial injection-barrier change, which in turn can be related to highly electronegative F asymmetrically positioned in PFBT to create strong dipoles.[35] We will revisit this statement in Section 2.4.

The SAMs also significantly influenced the mobility, as shown in μ_{ch} plot in Figure 3c (inset). Even with smaller grains (Figure 2a and b), the DNTT film in the BC-SAMs device exhibited better transport quality than that in the BC sample. A recent report on organic diodes on PFBT-Au also showed smaller but better-ordered and larger-mobility pentacene grains on SAMs.[36] It is therefore inferred that the classical grain-size dependence of the mobility may be reversed in cases where metal-induced frustration plays an important role. Therefore, the whole analysis up to this point delivers a solid understanding that the performance improvement by the SAMs, first viewed as enhanced I_D in Figure 1c, arises in fact from both decreased R_c and increased μ_{ch}, with fairly comparable contribution.

The TC potential profiles had $V_c = 0$, and therefore μ_{ch} is calculated by replacing V_{ch} with V_D in Equation (3) and (4). The values of μ_{ch} for all three structures are then compared to the mobility extracted by derivative-based methods:

$$\mu_{lin} = -\frac{dI_D}{dV_G} \times \frac{L}{W} \times \frac{1}{C} \times \frac{1}{V_D}, \quad (5)$$

$$\mu_{sat} = \left(\frac{d\sqrt{-I_D}}{dV_G}\right)^2 \times \frac{2L}{W} \times \frac{1}{C}. \quad (6)$$

Here, μ_{lin} and μ_{sat} correspond to the linear- and saturation regime mobility, measured at small and high V_D, respectively. Since all three methods apparently accommodate the V_G dependence of the mobility, we took the maximum over the gate-sweep range as representative for each device, to present in Figure 3d the full comparison performed on the exactly same set of transistors (5 FETs for each group). It is clear from this plot that the choice of method strongly affects the extracted mobility and the degree/direction of inter-method changes may reflect non-idealities of the devices. When considering potentiometrically verified μ_{ch} as the exact value, the widely cited μ_{sat} values underestimate the mobilities for the BC and BC-SAMs devices and overestimate for the TC device; the ratio μ_{sat}/μ_{ch} is 0.48 for the BC, 0.37 for the BC-SAMs, and 1.3 for the TC OFETs. It is worth mentioning that our TC OFETs featured a nearly straight square-root I_D versus V_G plot (Figure S5, Supporting Information), while not exempt from possible overestimation.[15] We point out that the problem originates fundamentally from the specificities of the derivative-based method itself, which systematically neglects the $d\mu/dV_G$ (and related terms) to reach a simple and applicable expression for mobility.[34] After all, the impressive linearity between the square-root I_D and V_G for the TC devices confirms the outstanding ability of DNTT to form well-ordered molecular films (Figure 2c) with strong electronic coupling between frontier orbitals.[37,38]

2.4. Physical Description

When we encounter strongly contact-limited devices, it is important to understand material and structural origins of R_c, to identify the most meaningful strategies for improvements. In staggered devices, it is believed that the bulk film resistance (also known as the access resistance) contributes mostly, as the injected carriers need to travel vertically to reach the channel.[39,40] In this case, the metal/organic carrier-injection barrier seems to have minimal effect.[25] The coplanar OFETs, meanwhile, are sensitively affected by the barrier height, while the semiconductor mobility still is an important factor.[26]

Now that we know the accurate values for μ_{ch} and R_c, we can further our analysis to gain deeper understanding of R_c. As a sharp carrier-density bottleneck region is responsible for R_c in coplanar devices,[25] R_c in our BC and BC-SAMs OFETs can basically expect twofold influences from V_G; firstly as the charge-density modulator (capacitive effect), secondly as the mobility changer within the same R_c zone. In fact, by multiplying μ_{ch} with V_G-V_T, we build an effective input variable that take both effects into account. **Figure 4**a proves that R_c scales quasi-linearly with this variable, and more importantly, a collective behavior is seen for different devices. Based on this finding, a simple analytical description that correlates R_c with other parameters can be proposed as

$$R_c = -\frac{\beta}{\mu_{\text{ch}}\left(V_G - V_T\right)}, \qquad (7)$$

where β is the proportionality constant. From a physical point of view, the parameter β should contain, among others, a capacitance term that dictates the efficiency of charge accumulation and an injection-barrier term that directly probes the metal/organic junction. The fitting results in Figure 4b globally validate this inverse proportionality, with some unexpected and interesting features. Firstly, different OFETs from the same chip can be overall well described by a single trend line. This aspect is clear for the five BC OFETs that are fully fitted with $\beta = 3.1 \times 10^7$ F^{-1}cm^2. It means that the major reason for device-to-device non-uniformity is the local mobility (or morphological) variation, while the injection barrier (contained in β)

remains rather stable across the samples. Secondly and more surprisingly, the BC-SAMs devices also visibly satisfy the same trend at sufficiently high V_G, which starts to deviate at small V_G. As a model system for fluorinated aromatic SAMs, PFBT can exert morphological and energetic effects.[13] Figure 4b suggests that, in this particular group of transistors, the SAM effect more strongly manifests itself as a growth template (Figure 2b) and a boost for the mobility (Figure 3d), while its effect on injection energy (or β) was weaker. In other words, the reduced R_c in the SAM-functionalized OFETs is mainly due to the increase in μ_{ch}, which in the end drove the overall performance enhancement (Figure 1c). The deviation at small V_G, for which a boundary with a smaller β can be drawn, may indicate that possible (yet still non-dramatic) barrier reduction comes into play when fewer accumulated charges become available, but further investigation seems necessary to fully understand this behavior.

3. Conclusion

Organic semiconductors have many appealing potential applications, but some of their distinct characteristics fundamentally limit device performances. Insignificant generation of thermal carriers and pronounced Fermi-level pinning are among such features, both of which make practical devices often contact-dominated. We have comprehensively revisited the origins, manifestations, and impacts of R_c in DNTT OFETs. Particular attention was paid to different approaches to extract charge-carrier mobility, and it became evident that those which do not address R_c (ideal MOSFET model) or do not determine V_T explicitly (derivative-based methods) should not be preferred. It can be pointed out that taking full account of the effects of R_c is highly recommended when reporting on OFETs with new materials and/or device structures. SKPM provides the invaluable capability to separate contact effects from the channel on a single device, without having to compare several devices in which comparability (and reproducibility) of devices can be a significant issue. Further understanding was established on the electrode SAMs. At the interface between PFBT and DNTT, the promoted molecular packing and enhanced transport was shown to create major contribution to the

performance improvement. We infer that preparing SAMs that further optimize the molecular arrangement of DNTT may eventually lead to BC devices whose performance approaches that of the TC counterparts.

4. Experimental Section

Device Fabrication: The OFETs were fabricated according to the structures in Figure 1a. Heavily doped *n*-type Si wafers with 100-nm thick thermally grown SiO_2 were used as gate substrates. They were cleaned with acetone, isopropanol, and dried with nitrogen blow. After brief oxygen plasma treatment, a PMMA solution (M.W. = 120,000, 40 mg/mL in toluene) was spin-coated at 2000 rpm for 45 s, and annealed at 120°C for 30 min (film thickness: 200 nm). For the BC and BC-SAMs devices, a 5-nm Cr adhesion layer and 35-nm Au source/drain electrodes were thermally evaporated. The SAMs were anchored by immersion into a 10 mM PFBT solution (in isopropanol) for 10 min, followed by rinsing with pure isopropanol and drying with nitrogen. The organic channel was deposited simultaneously for all devices, by thermal evaporation of DNTT at 0.2 Å/s with the final nominal thickness of 40 nm. For the TC OFETs, 30-nm Au source/drain electrodes were vacuum-deposited on the semiconductor. For each evaporation step, a dedicated shadow mask was used to make patterns. The channels have $W = 500$ μm and $L = 50$ μm. All chemicals were used as-received from Sigma-Aldrich.

Electrical Characterization: The current-voltage characteristics of the OFETs were recorded using a Keithley 4200 Semiconductor Characterization System. The measurements were carried out in the dark and under ambient atmosphere.

AFM Measurement: The surface morphology of the DNTT films was investigated by tapping-mode AFM (XE-100, Park Systems). The image analysis was performed using the Gwyddion software.

SKPM Measurement: Topographic and surface potential measurements were performed in a 2-step scan mode (Bruker Nanoscope III). Electrode potentials were switched off for topography scans and applied for the interlaced lift mode scan, in which the tip is raised so

that van der Waals interactions with the surface are negligible. Potential profiles shown in

Figure 3 are the background-referenced data obtained by subtracting the profiles with $V_D = 0$

V from the profiles with each non-zero V_D. Due to the high surface roughness (Figure 2 a and

b), measured profiles were smoothed for the BC and BC-SAMs devices to clarify the overall

curve shapes.

Supporting Information
Supporting Information is available from the Wiley Online Library or from the author.

References

[1]   G. Dennler, *Mater. Today* **2007**, *10*, 56.

[2]   D. Choi, P.-H. Chu, M. McBride, E. Reichmanis, *Chem. Mater.* **2015**, *27*, 4167.

[3]   K. D. G. I. Jayawardena, L. J. Rozanski, C, A, Mills, S. R. P. Silva, *Nat. Photonics*
2015, *9*, 207.

[4]   E. Zimmermann, P. Ehrenreich, T. Pfadler, J. A. Dorman, J. Weickert, L. Schmidt-
Mende, *Nat. Photonics* **2014**, *8*, 669.

[5]   C.-H. Kim, Y. Bonnassieux, G. Horowitz, *IEEE Trans. Electron Devices* **2014**, *61*,
278.

[6]   H. Sirringhaus, *Adv. Mater.* **2014**, *26*, 1319.

[7]   G. Horowitz, P. Lang, M. Mottaghi, H. Aubin, *Adv. Funct. Mater.* **2004**, *14*, 1069.

[8]   P. V. Pesavento, R. J. Chesterfield, C. R. Newman, C. D. Frisbie, *J. Appl. Phys.* **2004**,
96, 7312.

[9]   S. D. Wang, T. Minari, T. Miyadera, K. Tsukagoshi, Y. Aoyagi, *Appl. Phys. Lett.* **2007**, *91*, 203508.

[10]   P. Marmont, N. Battaglini, P. Lang, G. Horowitz, J. Hwang, A. Kahn, C. Amato, P. Calas, *Org. Electron.* **2008**, *9*, 419.

[11]   Y. Xu, T. Minari, K. Tsukagoshi, J. A. Chroboczek, G. Ghibaudo, *J. Appl. Phys.* **2010**, *107*, 114507.

[12]   F. Ante, D. Kälblein, T. Zaki, U. Zschieschang, K. Takimiya, M. Ikeda, T. Sekitani, T. Someya, J. N. Burghartz, K. Kern, H. Klauk, *Small* **2012**, *8*, 73.

[13]   C.-H. Kim, H. Hlaing, J.-A. Hong, J.-H. Kim, Y. Park, M. M. Payne, J. E. Anthony, Y. Bonnassieux, G. Horowitz, I. Kymissis, *Adv. Mater. Interfaces* **2015**, *2*, 1400384.

[14]   J.-m. Cho, T. Mori, *Phys. Rev. Appl.* **2016**, *5*, 064017.

[15]   E. G. Bittle, J. I. Basham, T. N. Jackson, O. D. Jurchescu, D. J. Gundlach, *Nat. Commun.* **2016**, *7*, 10908.

[16]   S. Yogev, R. Matsubara, M. Nakamura, U. Zschieschang, H. Klauk, Y. Rosenwaks, *Phys. Rev. Lett.* **2013**, *110*, 036803.

[17]   Y. Yamagishi, K. Kobayashi, K. Noda, H. Yamada, *Appl. Phys. Lett.* **2016**, *108*, 093302.

[18]   G. de Tournadre, F. Reisdorffer, R. Rödel, O. Simonetti, H. Klauk, L. Giraudet, *J. Appl. Phys.* **2016**, *119*, 125501.

[19]   C. H. Kim, A. Castro-Carranza, M. Estrada, A. Cerdeira, Y. Bonnassieux, G. Horowitz, B. Iñiguez, *IEEE Trans. Electron Devices* **2013**, *60*, 1136.

[20]   P. V. Necliudov, M. S. Shur, D. J. Gundlach, T. N. Jackson, *J. Appl. Phys.* **2000**, *88*, 6594.

[21]   M. Estrada, A. Cerdeira, J. Puigdollers, L. Reséndiz, J. Pallares, L. F. Marsal, C. Voz, B. Iñiguez, *Solid-State Electron.* **2005**, *49*, 1009.

[22]   T. Sakanoue, H. Sirringhaus, *Nat. Mater.* **2010**, *9*, 736.

[23] H. Yagi, T. Miyazaki, Y. Tokumoto, Y. Aoki, M. Zenki, T. Zaima, S. Okita, T. Yamamoto, E. Miyazaki, K. Takimiya, S. Hino, *Chem. Phys. Lett.* **2013**, *563*, 55.

[24] U. Zschieschang, F. Ante, D. Kälblein, T. Yamamoto, K. Takimiya, H. Kuwabara, M. Ikeda, T. Sekitani, T. Someya, J. Blochwitz-Nimoth, H. Klauk, *Org. Electron.* **2011**, *12*, 1370.

[25] C. H. Kim, Y. Bonnassieux, G. Horowitz, *IEEE Electron Device Lett.* **2011**, *32*, 1302.

[26] C. H. Kim, Y. Bonnassieux, G. Horowitz, *IEEE Trans. Electron Devices* **2013**, *60*, 280.

[27] R. Ruiz, D. Choudhary, B. Nickel, T. Toccoli, K.-C. Chang, A. C. Mayer, P. Clancy, J. M. Blakely, R. L. Headrick, S. Iannotta, G. G. Malliaras, *Chem. Mater.* **2004**, *16*, 4497.

[28] C. H. Kim, O. Yaghmazadeh, D. Tondelier, Y. B. Jeong, Y. Bonnassieux, G. Horowitz, *J. Appl. Phys.* **2011**, *109*, 083710.

[29] Y. Mei, D. Fogel, J. Chen, J. W. Ward, M. M. Payne, J. E. Anthony, O. D. Jurchescu, *Org. Electron.* **2017**, *50*, 100.

[30] T. Yamamoto, K. Takimiya, *J. Am. Chem. Soc.* **2007**, *129*, 2224.

[31] C.-H. Kim, H. Hlaing, M. M. Payne, K. G. Yager, Y. Bonnassieux, G. Horowitz, J. E. Anthony, I. Kymissis, *ChemPhysChem* **2014**, *15*, 2913.

[32] O. Kryvchenkova, I. Abdullah, J. E. Macdonald, M. Elliott, T. D. Anthopoulos, Y.-H. Lin, P. Igić, K. Kalna, R. J. Cobley, *ACS Appl. Mater. Interfaces* **2016**, *8*, 25631.

[33] A. Ortiz-Conde, F. J. García-Sánchez, J. Muci, A. Terán Barrios, J. J. Liou, C.-S. Ho, *Microelectron. Reliab.* **2013**, *53*, 90.

[34] M. Mottaghi, G. Horowitz, *Org. Electron.* **2006**, *7*, 528.

[35] Z. Jia, V. W. Lee, I. Kymissis, L. Floreano, A. Verdini, A. Cossaro, A. Morgante, *Phys. Rev. B* **2010**, *82*, 125457.

[36] C.-m. Kang, J. Wade, S. Yun, J. Lim, H. Cho, J. Roh, H. Lee, S. Nam, D. D. C. Bradley, J.-S. Kim, C. Lee, *Adv. Electron. Mater.* **2016**, *2*, 1500282.

[37]   D. Venkateshvaran, M. Nikolka, A. Sadhanala, V. Lemaur, M. Zelazny, M. Kepa, M. Hurhangee, A. J. Kronemeijer, V. Pecunia, I. Nasrallah, I. Romanov, K. Broch, I. McCulloch, D. Emin, Y. Olivier, J. Cornil, D. Beljonne, H. Sirringhaus, *Nature* **2014**, *515*, 384.

[38]   Y. Hasegawa, Y. Yamada, T. Hosokai, K. R. Koswattage, M. Yano, Y. Wakayama, M. Sasaki, *J. Phys. Chem. C* **2016**, *120*, 21536.

[39]   D. Natali, M. Caironi, *Adv. Mater.* **2012**, *24*, 1357.

[40]   C. Liu, Y. Xu, Y.-Y. Noh, *Mater. Today* **2015**, *18*, 79.
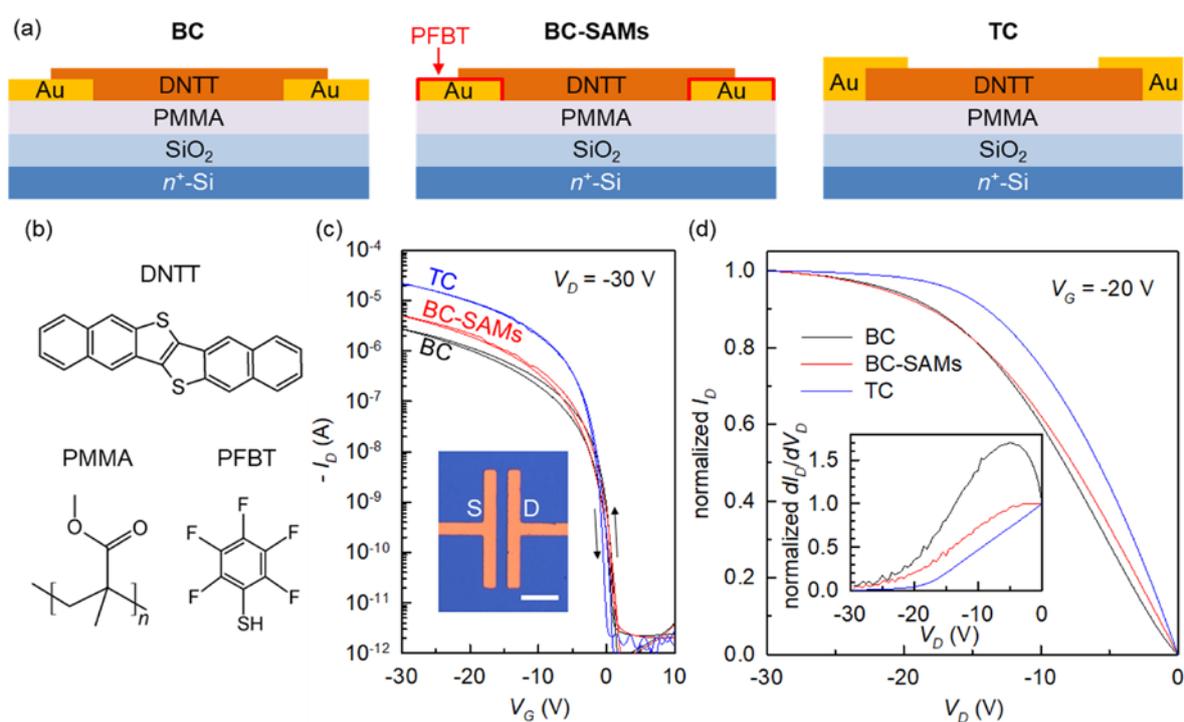
Figure 1. (a) Structural illustration of the three OFET geometries employed in this study. (b) Chemical structure of DNTT, PMMA, and PFBT. (c) Saturation-regime dual-sweep transfer characteristics of OFETs. Inset: microscope image of the source (S) and drain (D) electrodes in the channel area (scale bar: 150 μm). (d) Normalized output curves revealing the ideality of each transistor group. Inset: Normalized differential output conductance.
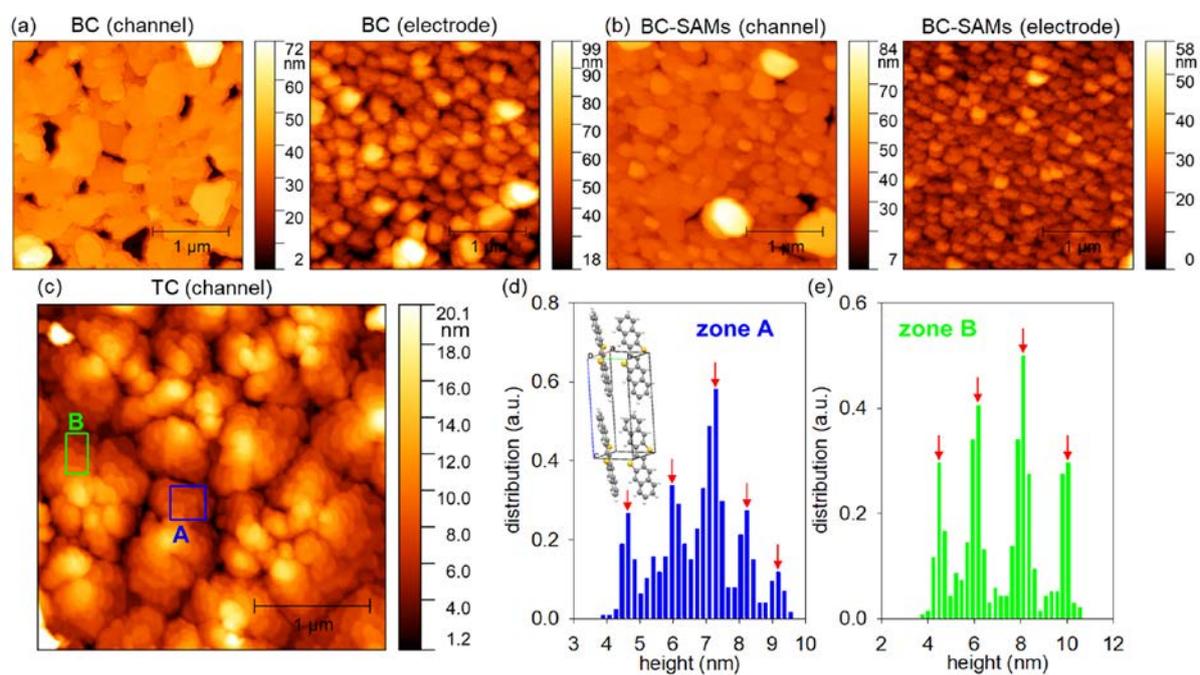
Figure 2. AFM topography of the DNTT film in (a) BC, (b) BC-SAMs, and (c) TC OFETs. For the BC and BC-SAM samples, images were separately taken on the channel and the electrode region. (d) and (e) correspond to the height histograms analyzed in zone A and B in (c). The arrows indicate the peaks that evidence existence of molecular terraces and layered structure. Inset of (d): molecular packing motif of DNTT crystals.
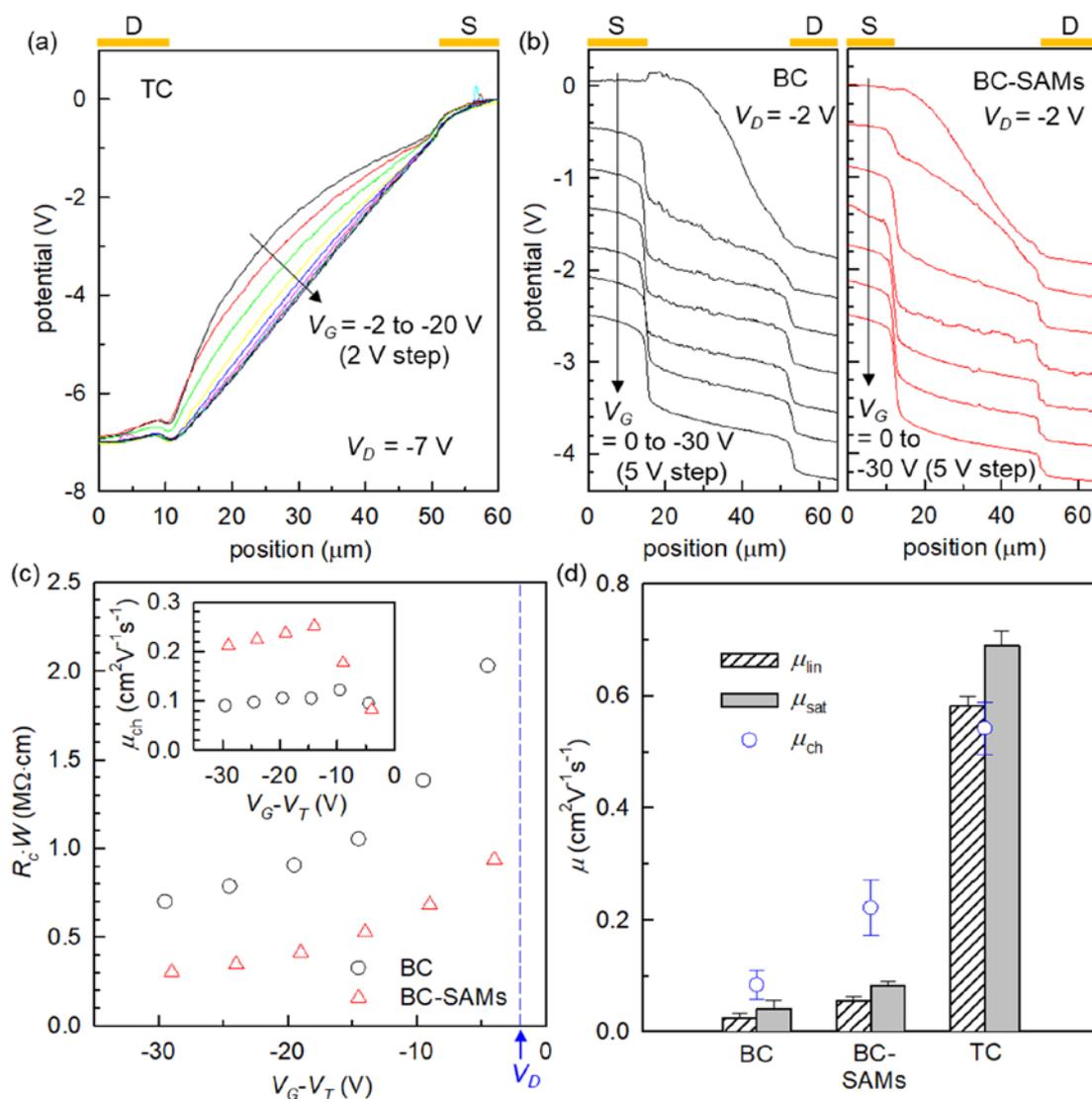
Figure 3. (a) Potent profiles measured on the TC OFET with an intermediate V_D and varying V_G. D and S show the position of the drain and the source electrode, respectively. (b) Potential profiles measured on the BC (left) and BC-SAMs (right) devices with a small V_D (linear regime) and varying V_G. Vertical data offsets were introduced to clarify the shape of each graph. (c) V_G-dependent $R_c \cdot W$ (main panel) and μ_{ch} (inset) of representative BC and BC-SAM devices. (d) Comparison of charge-carrier mobility calculated by different methods.
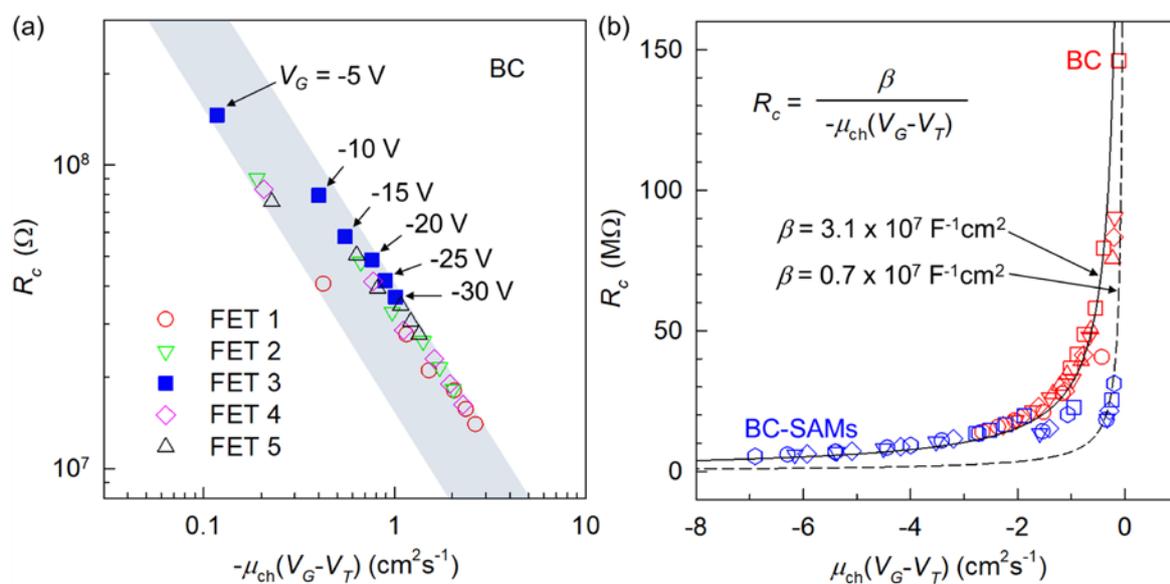
Figure 4. (a) Log-log R_c versus $-\mu_{ch}(V_G-V_T)$ plot for five BC OFETs. The results from a selected device (FET 3) are highlighted with filled symbols and the corresponding V_G values are given for this device. (b) Linear plot for five BC (red) and five BC-SAMs (blue) devices (different FETs have different symbols). The experimental data are compared to an inverse proportional function.

Contact properly: DNTT is an outstanding organic hole-transporter, but its low-lying HOMO makes the material prone to poor injection. This research shows that strong interplay between these two factors brings substantial device non-idealities, and entails difficulties in performance evaluation. An SKPM-based analysis clarifies material origins, parametric interplays, and conceptual models for contacts in DNTT transistors.

Organic electronics

C.-H. Kim, S. Thomas, J. H. Kim, M. Elliott, J. E. Macdonald, M.-H. Yoon*

Potentiometric Parameterization of Dinaphtho[2,3-b:2′,3′-f]thieno[3,2-b]thiophene Field-Effect Transistors with a Varying Degree of Non-Idealities
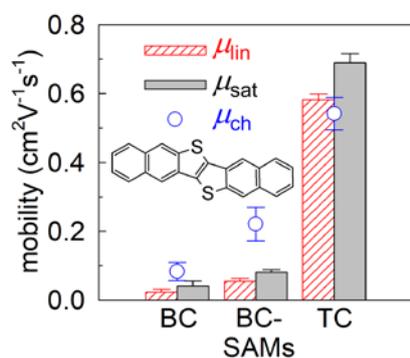
Supporting Information

Potentiometric Parameterization of Dinaphtho[2,3-b:2′,3′-f]thieno[3,2-b]thiophene Field-Effect Transistors with a Varying Degree of Non-Idealities

Chang-Hyun Kim, Suzanne Thomas, Ji Hwan Kim, Martin Elliott, J. Emyr Macdonald, and Myung-Han Yoon*
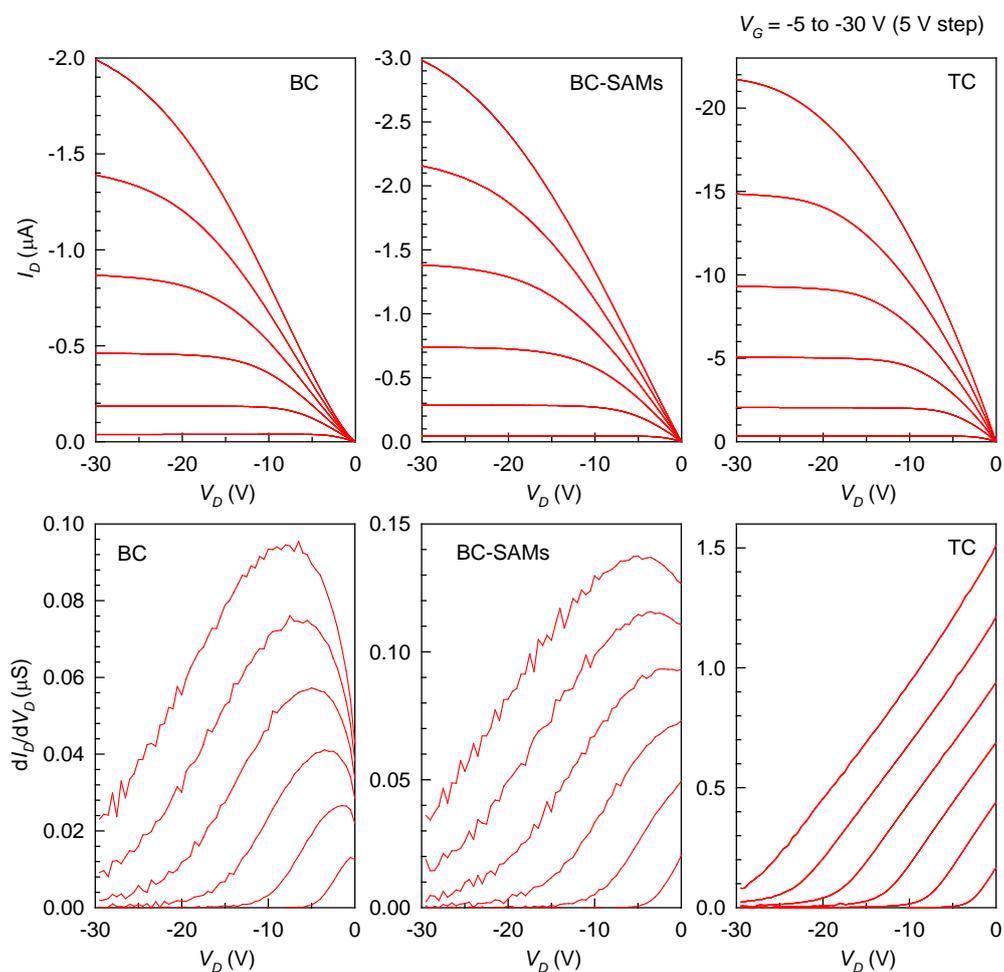
Figure S1. Output characteristics (top) and differential output conductance (bottom) for BC, BC-SAMs, and TC DNTT OFETs.
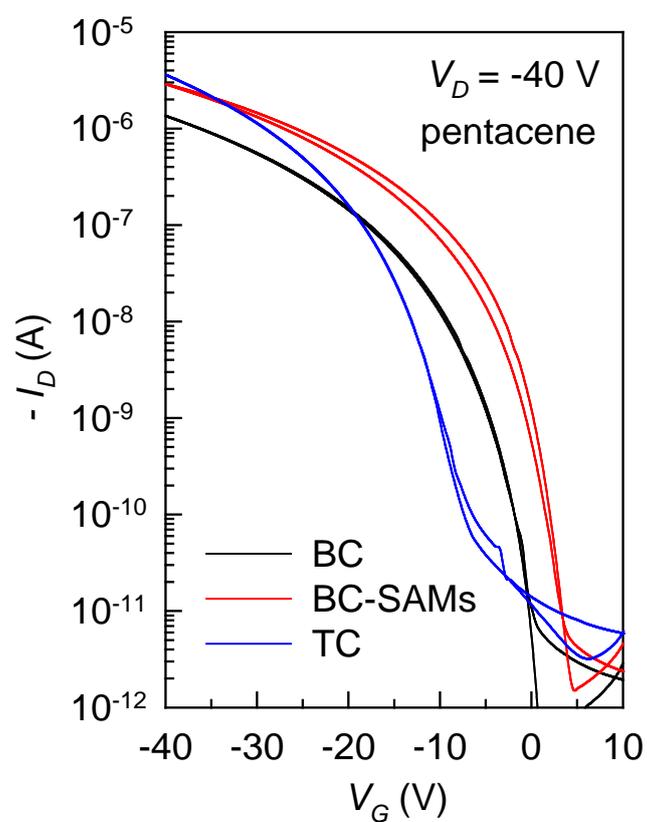
Figure S2. Saturation-regime transfer characteristics of the pentacene-based OFETs with the BC, BC-SAMs, and TC configuration.

(a)

(b)
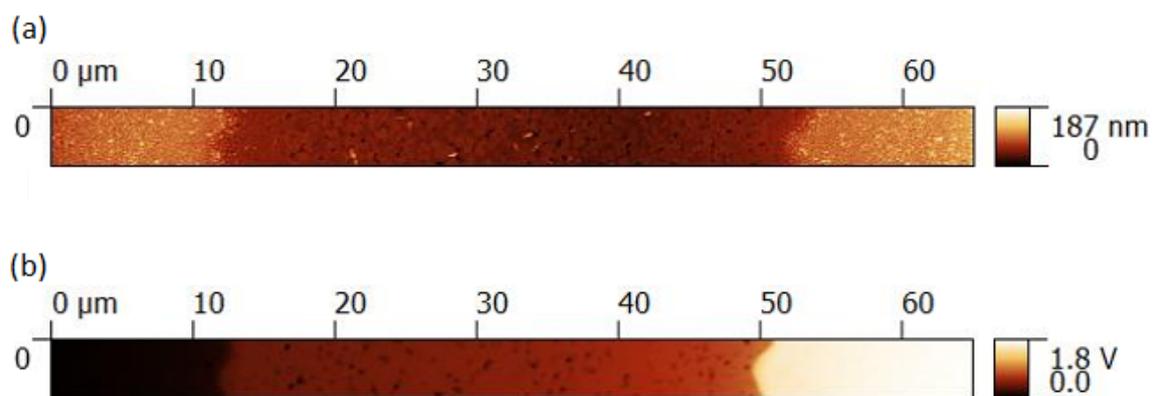
Figure S3. (a) Topography and (b) surface potential image of a BC OFET measured by SKPM. These images were taken at V_D = -2 V and V_G = -25 V.
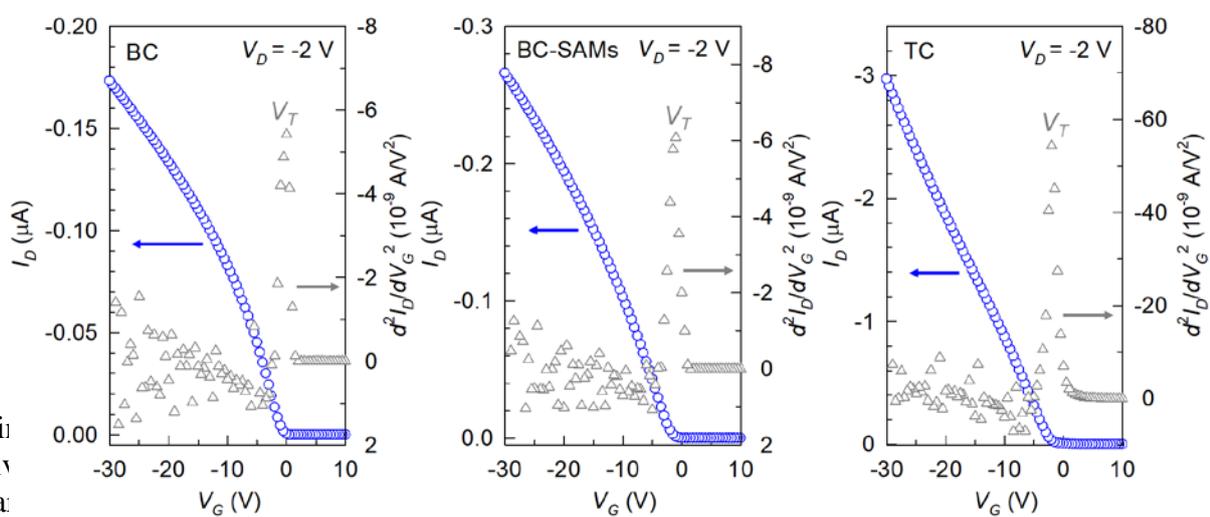
Figure S4. Lin...
order derivativ...
values of V_T a...
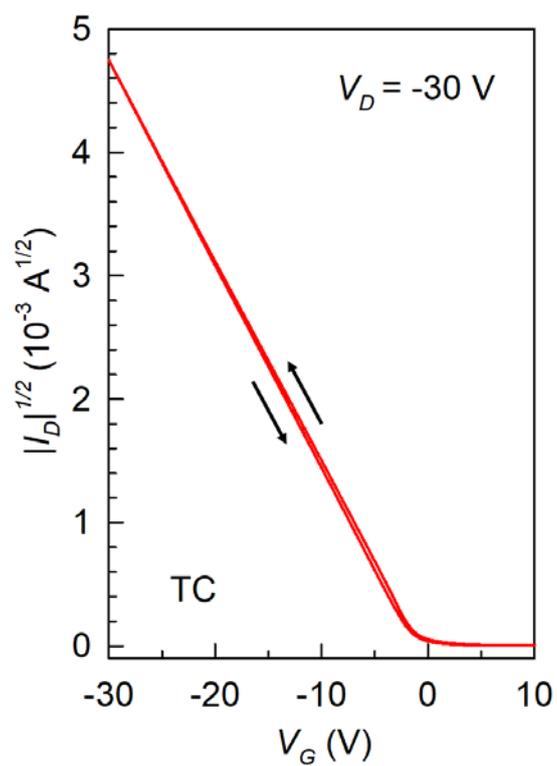
Figure S5. Square-root plot for the saturation-regime transfer characteristic of a representative TC OFET. The arrows indicate the direction of voltage sweep.